NJC

ROYAL SOCIETY OF CHEMISTRY

PAPER

View Article Online
View Journal | View Issue

Cite this: *New J. Chem.*, 2025, **49**, 18103

Oxygen activation on carbon-coated iron nanoparticles

Aleksandar Staykov

This work explores the feasibility of molecular oxygen activation and dissociation on the sp^2-hybridized carbon surface of carbon-coated iron nanoparticles. Using density functional theory with a generalized gradient approximation, we elucidate the geometry and electronic structure of these nanoparticles, highlighting the nature of the C–Fe binding interactions and the resulting modifications to the carbon surface electronic states. The enhanced catalytic activity of carbon induced by the underlying iron core is attributed to core–shell electronic interactions within the nanoparticles. Activation of molecular oxygen to superoxo and peroxo species was investigated using the nudged elastic band method, with electron transfer processes analyzed in detail and linked to the core–shell characteristics of the system. Additionally, we examined the effects of nitrogen doping in the carbon shell on the structural and electronic properties of the nanoparticles. Potential degradation pathways, including parasitic reactions during oxygen activation, were also identified. This study offers new theoretical insights into the functional behavior of Fe–C–N catalysts.

Received 16th July 2025,
Accepted 22nd September 2025

DOI: 10.1039/d5nj02903a

rsc.li/njc

Introduction

Recently, the widespread requirement of carbon neutral energy generation has been the driving force for the active advancement in energy-related material technologies for applications in fuel cells, solar cells, artificial photosynthesis devices, high-capacity Li-ion batteries, *etc.*[1] Among those, fuel cells are of great importance, owing to their ability to convert chemical energy to electricity without the environmentally harmful combustion process. A fuel cell consists of a fuel electrode, electrolyte, and an air electrode where the fuel oxidation, ionic transport, and oxygen reduction reactions take place, respectively. Depending on the materials used and the operating conditions, fuel cells are divided into solid oxide fuel cells (SOFCs) and polymer electrolyte membrane fuel cells (PEMFCs). Solid oxide fuel cells contain complex oxide electrolyte, in most cases with perovskite or Ruddlesden–Popper lattices, which conducts oxide ions through a vacancy hoping mechanism or through interstitial rock-salt layers.[2–5] Due to the high activation barriers for the oxide ion transport in perovskite lattices, SOFCs usually operate at high temperatures of ~1100 K. As a result, the high operating temperature of SOCFs provides the necessary activation energy for the fuel oxidation and oxygen reduction reactions, thus, those devices can operate without expensive catalysts. Another advantage of the high operating temperature is the low selectivity of SOFCs towards the fuel composition, allowing them to operate with low-purity hydrogen gas, hydrocarbons, alcohols, *etc.* Nevertheless, the high temperature is the reason for various degradation mechanisms of SOFCs such as cracks and fractures within the electrolyte, delamination of the electrodes, and ionic segregation on the electrode surfaces, which lead to a significant drop in device performance.[6,7] Major research into SOFC operating materials focuses on the search for oxide ion conductors that can operate at lower temperatures ~900 K. Such low temperatures can be achieved by elemental doping of the perovskites, which leads to increased concentration of oxide ion vacancies. Another approach is to use proton conducting complex oxides. Owing to the lower activation energy required for the proton transport, proton conducting oxides are expected to further lower the operating temperature of SOFCs.[8]

PEMFCs operate at significantly lower temperatures (~400 K) compared to SOFCs. Thus, they exhibit higher durability and can find applications in home appliances and fuel cell vehicles. They usually contain an organic polymer membrane as an electrolyte, which enables proton transport between the electrodes. A widely used electrolyte for PEMFCs is Nafion,[9] however, due to its high cost, active research is focused on the search for cheaper materials such as nano-cellulose and various crosslinked polymers.[10–12] Due to the low operating temperature, PEMFCs require active catalysts for the fuel oxidation and oxygen reduction reactions.[13] Platinum nanoparticles, and other precious metals, were employed as major catalysts for the oxygen reduction reaction.[14,15] The use of precious metals significantly increases the cost and limits widespread use of the fuel cell technology. Also, metal nanoparticles are known to aggregate with time,

International Institute for Carbon-Neutral Energy Research I2CNER, Kyushu University, Fukuoka, 819-0395, Japan. E-mail: alex@i2cner.kyushu-u.ac.jp

which a main reason for the electrodes' degradation.[16] Larger nanoparticles have a lower surface area per gram precious metal and lead to electrodes with lower activity. Thus, the development of non-precious metal catalysis for PEMFCs is an important research field in modern electrochemistry.[17–20] While many (non-precious) transition metals, such as iron, nickel, cobalt, and copper, show good catalytic activity towards oxygen reduction, their surfaces easily oxidize and deactivate.

As a result, recent research was directed towards metal-free or low-metal loading catalysts based on graphitic carbon foams.[20,21] Those carbon foams possess irregular structures with a high concentration of sp^2-hybridized carbon atoms.[22] They are usually prepared by pyrolysis of small organic molecules and depending on their elemental content, dopants can be introduced into the graphene-like carbon material.[22] The possible dopants include nitrogen, phosphorous, boron, and sulfur. It was suggested that the dopants have an effect on the carbon foam catalyst's oxygen reduction catalytic activity.[23] Several studies argue that the oxygen reduction reaction could be completely catalyzed by metal-free catalysts.[24,25] The catalytic activity was related to defects in the sp^2-carbon network and different nitrogen centers such as graphitic nitrogen or pyridinic nitrogen site. However, it is widely believed that iron traces remain in the carbon catalyst and it is rather possible that those remaining iron centers are the actual active sites for the oxygen reduction.[17,20] Those iron atoms do not form nanoparticles of metallic iron (which is easily oxidized) but instead are coordinated in a porphyrin-like structure within defect sites in the graphene lattice where single iron centers exist in their cationic forms.[20,26] That model of the catalysts' active sites was created in analogy with various active sites in organometallic and bio-enzymatic chemistry (including the structure of hemoglobin) where strongly coordinated Fe(II) and Fe(III) centers can bind and activate molecular oxygen to superoxo and peroxo species followed by sequential oxygen–oxygen bond cleavage and formation of product compounds. In those models a single iron center is usually coordinated by three or four pyridinic or pyrrolic nitrogen atoms.[20,27]

High resolution tunneling electron microscope images reveal that beside single atom centers, iron is present in the form of metal nanoparticles with a size of 1–20 nm coated with one to several layers of graphene-like carbon.[28] Those nanoparticles have a layered onion-like structure[29,30] of carbon shells with metallic iron in the core and they are believed to be catalytically inert. A recent study shows that those carbon coated iron nanoparticles can enhance the catalytic activity of nearby porphyrin-type single iron atom active sites.[31] That observation opened the question of the structure and electronic properties of carbon-coated iron nanoparticles and the mechanism of enhanced oxygen reduction activity in their vicinity.

A recent study[21] demonstrated a procedure for poisoning of all surface-exposed iron centers. As a result, the porphyrin-like active sites have been successfully deactivated. Although it was expected that as a result of the poisoning the catalytic activity towards oxygen reduction would drop, the catalyst could maintain its properties. That result was an important hint that the system contains a different type of active sites that should not contain surface-exposed iron atoms. In this study we will investigate the ability of 1–2 nm carbon coated iron nanoparticles to activate molecular oxygen to its superoxo and peroxo states using first-principle methods. We will investigate the surface electronic properties of the carbon shell and the effect of the core iron atoms on the carbon shells.

Carbon coated iron nanoparticles and iron clusters encapsulated in single wall carbon nanotubes have been studied previously theoretically using density functional theory. Taubert and Laasonen[32] investigated the geometry of C180 fullerene coated Fe55 nanoparticles. They showed that the fullerene and the nanoparticle exhibit icosahedron symmetry. They studied the energy difference between carbon coated nanoparticles with high symmetry (icosahedron) and lower symmetries showing that the high-symmetry geometry is energetically favored. In the optimized geometry an apex iron atom is pointing towards the center of the five-member ring of the fullerene. In addition, they estimated the magnetic properties of the clusters.

Computational methods

Periodic, plane wave density functional theory (DFT) calculations and first principle molecular dynamics were performed with the Vienna ab initio Software Package (VASP). The Perdew–Burke–Ernzerhof (PBE) exchange–correlation functional was applied using projector augmented wave (PAW) pseudopotentials.[33–36] Selected systems have been recalculated with the R2SCAN metaGGA functional and the results show similar qualitative trends to PBE. However, due to convergence difficulties with R2SCAN, PBE was selected throughout the study. Electron energies were converged to 10^{-6} eV using a Gaussian smearing method with Sigma 0.0025. The calculations were performed with a 450 eV cut-off energy and gamma *k*-points mesh. The cut-off energy was converged in the range of 300 eV to 500 eV and steps of 5 eV with the total energy difference between two sequential steps falling below 0.001 eV. All calculations were spin polarized and the spin state of the carbon-coated iron nanoparticles was estimated. The valence electron configuration for carbon was $2s^22p^2$, for nitrogen $2s^22p^3$, and for iron $3d^74s^1$ while the core electrons were simulated in the pseudopotential. Geometry optimization was performed using the conjugated gradient algorithm. The relaxation was performed for the atomic positions only until the forces converged to values below 0.03 eV $Å^{-2}$. Activation barriers for chemical reactions were determined using the nudged elastic band (NEB) method where the band was relaxed to forces below 0.03 eV $Å^{-2}$. During the NEB optimization the spin state was relaxed, and spin crossover processes were observed during the oxygen reduction reaction. Charge analysis was performed using the Bader method.[37] In addition, electron density difference maps were employed to elucidate the electron flow between carbon and iron, as well as between carbon-coated iron clusters and oxygen molecules. Binding energies were calculated to elucidate the strength of

adsorption of oxygen on carbon surfaces and to estimate the strength of interaction between the iron core and carbon shell for carbon-coated iron clusters. The binding energy is calculated as the difference between the energy of carbon–iron nanoparticles (optimized) and the sum of the energies of the carbon shell (single point calculation) and the iron core (single point calculation) as shown in eqn (1). The geometry of the carbon shell is obtained from the geometry of the carbon–iron nanoparticle with the iron core deleted. The geometry of the iron core is obtained from the geometry of the carbon–iron nanoparticle with the carbon shell deleted.

$$\text{Binding energy} = E_{\text{carbon–iron np}} - (E_{\text{carbon shell}} + E_{\text{iron core}}) \quad (1)$$

Spin density maps were plotted using the difference between the majority and minority spin electron densities. The Bader analysis was used to assign spin density at the atom centers.[37] Throughout this study, the VESTA graphical visualization package was used.[38] Workfunction calculations were performed as the difference between the Fermi level and the vacuum level. The Fermi level was obtained from the DFT calculations. The vacuum level was obtained by plotting the average Hartree potential along the cell with the nanoparticle in the center. The vacuum level was taken at the flat region at the boundary of the periodic cell, equally far from the centered nanoparticles.

Results and discussion

We start the study with a minimalistic theoretical model of carbon coated iron nanoparticles. This kind of model allows for precise understanding of the iron/carbon integration at the first-principle level of theory. The model consists of a C60 buckminsterfullerene molecule wrapped around a 13-atom iron cluster. C60 is the smallest member of the fullerene family of molecules forming a zero-dimensional spherical structure of sp^2 hybridized carbon atoms arranged in alternating six and five membered rings. The C60 surface can be seen as an infinite curved defective graphene surface with periodical repetition of five-member ring defects. The C60 molecule possesses icosahedral symmetry with only two non-equivalent carbon atoms. The 13-iron atom cluster, Fe13, is the smallest iron particle characterized with a well-defined three-dimensional structure that can be found for larger nanoparticles. The 13 iron atoms can be arranged in either cuboctahedron or icosahedron particles with lower energy estimated for the icosahedron isomer. The icosahedron symmetry match of the iron cluster and the C60, as well as their optimal size, allows construction of a core–shell model of a carbon coated iron nanoparticle, C60@Fe13. To maintain the icosahedral symmetry, every iron atom from Fe13 points to the center of a five-carbon atom ring from the C60 inner surface. The interaction between Fe and the five-carbon atom ring is well-known from the structure of ferrocene with a formulae $Fe(C_5H_5)_2$. The model of C60@Fe13 is shown in Fig. 1A. The model is calculated as the C60@Fe13 particle is placed in a periodic cubic box with a side of 15 Å. As the particle size is roughly 1 nm, such model would allow a distance of 1 nm between particles in neighboring cells.

Geometry optimization and electronic properties of C60@Fe13 were calculated and the results are summarized in Fig. 1B. The bond lengths between the surface carbon atoms are 1.54 Å, which is longer than the 1.4 Å bond length in the

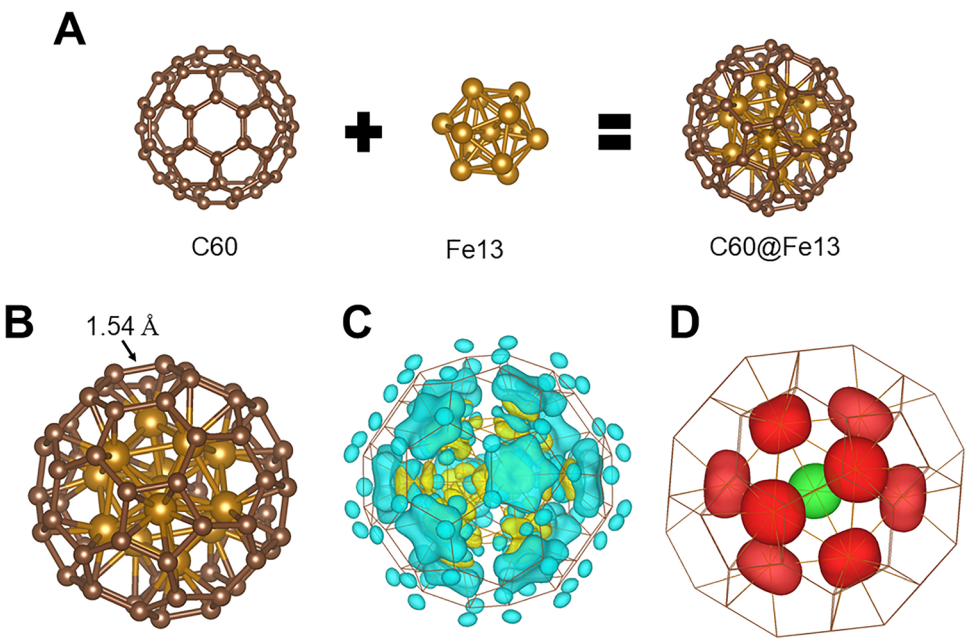

Fig. 1 Computational model, structural, and electronic properties of C60@Fe13. (A) Computational model; (B) optimized geometry; (C) electron density difference map. Blue color denotes positive electron density while yellow color denotes negative electron density; (D) spin density map. Red color denotes majority spin density, while green color denotes minority spin density.

isolated C60 molecule. The bond elongation suggests that electron density was transferred to the antibonding π* orbital of C60 leading to repulsive interaction between the carbon atoms. Electron density partition per ion-nucleus was performed following the Bader model.[37] The results showed that the iron core is deficient with 7 electrons which were transferred to the carbon shell. The result was expected due to the higher electronegativity of carbon compared to iron and also it follows the trend of positive core–negative shell charge separation in nanometer size metal clusters.[39] Electron density difference maps between the iron core and the carbon shell were used to understand the nature of core/shell charge separation. The results are summarized in Fig. 1C where a blue color was used to denote positive electron density, while a yellow color was used to denote regions deficient of electron density. The analysis shows that, as predicted from the particle geometry, the iron d_{z^2} AO provides electrons to the delocalized π-conjugated carbon network. Spin density is important to understand chemical processes which involve molecular oxygen and metallic iron. Thus, we have estimated that the particle is in a heptet spin state. The spin state was optimized during the SCF routine. Spin density maps are plotted in Fig. 1D, where a red color denotes electron density with majority spins, while a green color denotes electron density with minority spins. The majority spins were located on the 12 outer iron atoms while the minority spin is located on the central iron atom. The spin density on the carbon atoms was negligible. As can be seen from Fig. 1D the main magnetization remains on the iron core. The DOS plot in Fig. 2 reveals that spin density was transferred to the carbon shell. To gain quantitative understanding for this spin transfer, Bader population analysis was performed on the spin density volumetric data. The total spin density delocalized over the 60 carbon atoms was 0.38 electrons aligned ferromagnetically. The binding energy between the carbon shell (C60) and the iron core (Fe13) was calculated to be −11.39 eV showing that the composite nanoparticle is thermodynamically stable.

To understand the difference in the properties of the surface carbon atoms of C60@Fe13 compared with the carbon atoms of C60, we have calculated the workfunctions (WFs) and the density of states (DOS). The WF is defined as the energy difference between the Fermi level and the vacuum level. Both values were obtained from the DFT calculations. The WF of C60 was found to be 5.2 eV while the WF of C60@Fe13 was found to be 3.2 eV. This result suggests that C60@Fe13 would donate electron density more easily compared to C60 which is important for participation in oxygen reduction reactions. DOS plots of iron and carbon from C60@Fe13 and carbon C60 are compared in Fig. 2. All carbon atoms on the C60 surface possess equivalent electronic properties due to the high symmetry and the same is true for the carbon atoms on the surface of C60@Fe13. Additionally, the 12 outer iron atoms are also equivalent. Thus, for the DOS plots arbitrary carbon and iron atoms are chosen (excluding the central iron atom).

There is a significant difference between the C60's carbon atoms and the carbon atoms from the surface of C60@Fe13. C60's carbon atoms have the characteristic sp^2 carbon peaks while the carbon atoms from the C60@Fe13 surface show spin polarized minor peaks below the Fermi level. Careful examination of those peaks shows that they are identical to the d-band peaks of iron with only differences in the lower intensity. Those results suggest strong hybridization between the iron d-band and the delocalized π-conjugated bond of C60@Fe13. Thus, the iron d-band, responsible for the catalytic activity of iron would propagate to the nanoparticle surface mediated by the surface carbon atoms.

The hybridization of iron and carbon levels would have several consequences for the particle's catalytic properties. While metallic iron is a supreme catalyst for oxygen activation and dissociation reactions, the strong Fe–O bonding would lead to the formation of various iron oxides which would result in catalyst degradation. On its own, carbon wouldn't be able to dissociate oxygen under moderate conditions and at high temperature the reaction would lead to the formation of stable oxygen containing carbon derivatives and eventually to the formation of CO_2 (burning). Working in synergy, the carbon surface layer would protect the metallic iron from being oxidized, while the Fe–C hybridization provides the necessary catalytic sites on the carbon surface. In this way, a non-precious metal catalyst for the ORR would be realized taking advantage of the interfacial electronic interaction between iron and sp^2 carbon.

We have further investigated the interaction of triplet oxygen molecules with the carbon coated iron nanoparticles. Geometry optimization was performed for the oxygen molecule away from the particle surface and the oxygen molecule adsorbed on the

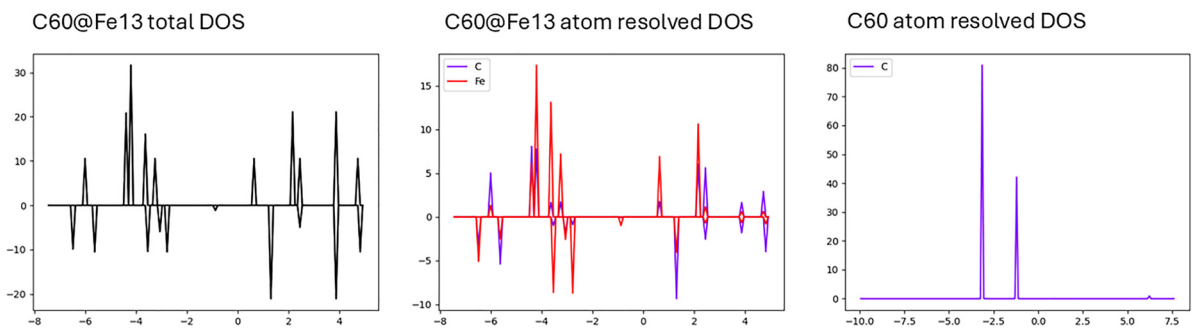

Fig. 2 DOS of iron and carbon atoms from C60@Fe13 and C60. Spin up and spin down states were plotted for C60@Fe13.

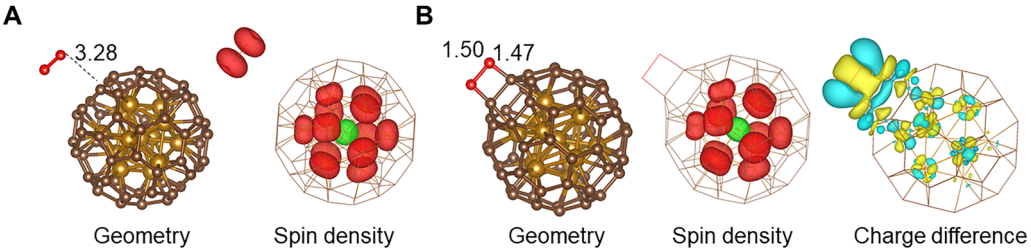

Fig. 3 Molecular oxygen interaction with C60@Fe13. (A) Away from the surface; (B) adsorbed on the surface. Blue color denotes positive electron density while yellow color denotes negative electron density. Red color denotes majority spin density, while green color denotes minority spin density. All distances are given in Å.

particle surface. The results are summarized in Fig. 3, where in Fig. 3A the optimized geometry and computed spin density map for oxygen away from the particle's surface are shown, and in Fig. 3B the optimized geometry, computed spin density map, and electron density difference map for oxygen adsorbed on the particle's surface are shown. In Fig. 3, the majority spin density is denoted with red color, while minority spin density is denoted with green color, and increased electron density is denoted with blue color while decreased electron density is denoted with yellow color.

At a distance of 3.3 Å away from the surface the oxygen molecule is in its triplet state with 1.22 Å distance between the two oxygen atoms. The spin state of the particle is heptet and there is no electron transfer between C60@Fe13 and the oxygen molecule. At a distance of 1.47 Å away from the surface the oxygen–oxygen bond elongates to 1.5 Å. Such elongation suggests that electron density has been transferred to the antibonding π^* orbitals of oxygen and the molecule has been activated either to the superoxo state, $O_2^{\bullet-}$, or the peroxo state, O_2^{2-}. Bader analysis was performed verifying that −1.7 electrons charge at the oxygen molecule. This result suggests that as a result of the adsorption the triplet oxygen molecule was transformed to the active peroxo species. This conclusion was further supported by the spin density map, showing no spin density at oxygen, *i.e.*, singlet spin state. In contrast, the superoxo state is a radical anion and would be characterized with doublet spin state on the oxygen molecule. The electron density difference map plotted in Fig. 3B shows that while there is interaction between the surface carbon atoms and the oxygen molecule, electron density has also been transferred from the iron d-orbitals within the nanoparticle core. This synergy for the electron transfer properties of surface carbon atoms and core iron atoms was demonstrated by the DOS plot in Fig. 1 where the iron d-band was hybridized with the carbon states. The binding energy between the peroxo species and the nanoparticle surface is −2.72 eV or −1.36 eV per C–O interaction. This energy shows that the activated oxygen molecule is strongly attached to the surface, however, an oxygen carbon covalent bond hasn't been formed. The typical C–O single bond has an energy of −3.71 eV.

To understand the reaction thermodynamics, we have performed NEB calculations between the starting (Fig. 3A) and ending (Fig. 3B) points for the oxygen activation reaction. The results are summarized in Fig. 4. The barrier for activation of

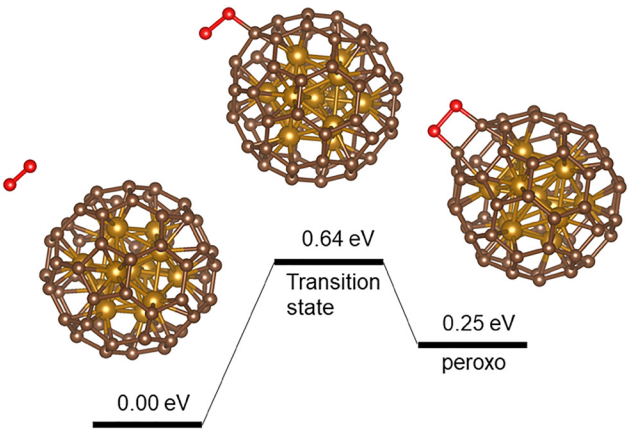

Fig. 4 Molecular oxygen interaction with C60@Fe13 obtained with the NEB method.

the molecular oxygen from its triplet state in the gas phase to the peroxo state on the carbon surface is 0.64 eV. That energy barrier shows that the reaction can proceed with reasonable rate at slightly elevated temperature, which corresponds to the operating conditions of PEMFCs. The reaction is endothermic with 0.25 eV. The endothermic reaction requires external driving force to proceed which can be either high temperature or applied bias. Our NEB calculation verifies that the activation of molecular oxygen on the carbon coated iron nanoparticle, C60@Fe13, is an energetically possible process under the operating conditions of PEMFCs.

We have further investigated the electronic properties and the geometry of the transition state for oxygen activation reactions. The results are summarized in Fig. 5 where the majority spin density is denoted with red color, while minority spin density is denoted with green color, and increased electron density is denoted with blue color while decreased electron density is denoted with yellow color. In the transition state geometry one of the oxygen atoms is bound to a surface carbon with a bond length of 1.49 Å. The oxygen–oxygen bond is elongated compared to the gas phase molecule to 1.41 Å. This bond is shorter than the bond of the peroxo oxygen and is close to the superoxo oxygen–oxygen bond length. The spin density analysis shows that the system has 7 unpaired electrons, 6 on the particle and one on the oxygen molecule situated on one of

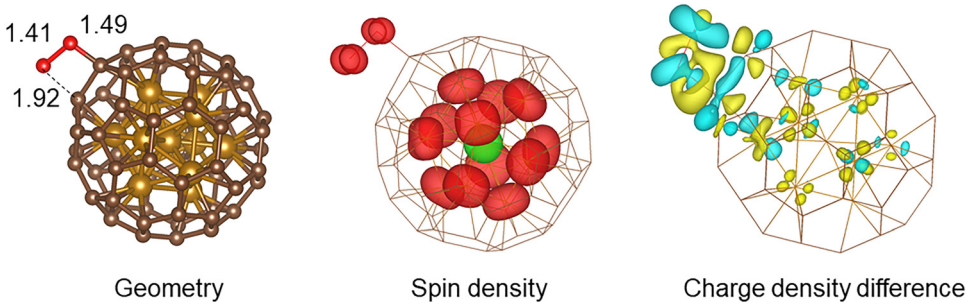

Fig. 5 Transition state geometry and electronic properties of molecular oxygen interaction with C60@Fe13. Blue color denotes positive electron density while yellow color denotes negative electron density. Red color denotes majority spin density, while green color denotes minority spin density. All distances are given in Å.

the antibonding π* molecular orbitals of oxygen. This result verifies that the transition state has the electronic properties of superoxo oxygen. The Bader population analysis shows that one electron has been transferred from the nanoparticle to the oxygen molecule. The electron density difference plot shows that the electron has been transferred from the iron core of the particle. Thus, we can conclude that on the surface of C60@Fe13, oxygen has been activated sequentially by one electron transfer to the superoxo state and second electron transfer to the peroxo state. The superoxo is a short living transition state while the peroxo is a stable product. The electrons have been transferred from the iron core of the nanoparticle through the surface carbon atoms. The binding energy between the superoxo species and the nanoparticle surface is −1.00 eV. This energy shows that the activated oxygen molecule is strongly attached to the surface, however, an oxygen carbon covalent bond hasn't been formed.

The catalytic activity towards oxygen activation of the Fe–C–N catalyst has often been discussed in relation to the nitrogen content.[40,41] Different studies have shown that increased nitrogen doping of the sp^2 hybridized carbon material might have beneficial effect on the catalytic activity.[40,41] The mechanism of these improved properties hasn't been revealed yet and could be related to additional catalytically active sites, changes in the electronic properties, *i.e.* workfunction lowering, or iron nanoparticles' size control by offering seeds for nanoparticle growth. Here, we investigate the effect of nitrogen on the proposed carbon coated iron nanoparticle catalyst. In our model a single nitrogen atom has been added to the carbon shell of the nanoparticle leading to configuration of C59N@Fe13. Our results show similar geometry and electronic properties with 7 electrons transferred from the iron core to the C59N shell. The binding energy between C59N and Fe13 is −9.95 eV, which is slightly lower compared to C60@Fe13. Nevertheless, C59N@Fe13 is a thermodynamically stable particle. The workfunction remained unchanged: 3.2 eV. The single nitrogen atom introduced a peak close to the Fermi energy in the nanoparticle's DOS. Such peak might lead to high reactivity or lower stability of the catalyst. We investigate the molecular oxygen interaction with the C59N@Fe13 surface. The results of the geometry optimization, spin density distribution, and electron density difference maps are plotted in Fig. 6. Fig. 6A summarizes the geometry and spin density of C59N@Fe13 with an oxygen molecule away from the surface, while Fig. 6B shows the geometry, spin density, and electron density difference of the oxygen molecule adsorbed onto the particle's surface. In Fig. 6, the majority spin density is denoted with red color, while the minority spin density is denoted with green color, and increased electron density is denoted with blue color while decreased electron density is denoted with yellow color.

Fig. 6 shows that the nitrogen atom in the carbon shell has the effect of reducing the spin density from 6 unpaired electrons to 5 unpaired electrons compared to the all carbon C60 shell. Thus, nitrogen will have an effect of reducing the magnetization of the nanoparticle catalyst. The major difference between the oxygen interaction with the surface of

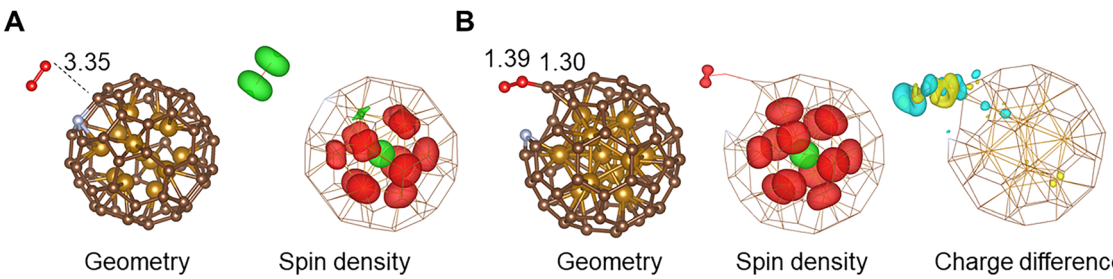

Fig. 6 Molecular oxygen interaction with C59N@Fe13. (A) Away from the surface; (B) adsorbed on the surface. Blue color denotes positive electron density while yellow color denotes negative electron density. Red color denotes majority spin density, while green color denotes minority spin density. All distances are given in Å.

C60@Fe13 and C59N@Fe13 is in the geometry of the adsorbed oxygen molecule. In the case of particle C59N@Fe13, the oxygen molecule cleaves the C–N bond on the nanoparticle's surface and binds to the dangling bond of the carbon atom leaving a pyridinic nitrogen site behind. As a result, the shell of the nanoparticle is damaged and iron atoms from the core are exposed to the surface. Analyzing the spin density in Fig. 6B, we can conclude that the nanoparticle has restored the spin state of 6 unpaired electrons typical for C60@Fe13. This suggests that by transferring the nitrogen atom from graphitic to pyridinic, its effect on the electronic properties of the nanoparticle has been diminished. Small spin density was estimated at the oxygen atom far from the surface. The estimated binding energy of the oxygen molecule to the particle surface is −2.93 eV. This energy is for a single C–O interaction. The computed binding energy is close to the average energy of a single C–O covalent bond (−3.71 eV). Thus, we can conclude that the nitrogen on the surface leads to degradation of the nanoparticle's shell and covalent bonding of the oxygen molecule, *i.e.*, oxidation of the nanoparticle's shell. The electron density difference map in Fig. 6B shows that electron transfer occurs only between the surface carbon atom and the oxygen molecule resulting in the formation of a covalent bond. Unlike nanoparticle C60@Fe13, for nanoparticle C59N@Fe13 there is no electron transfer from the Fe13 core to the surface oxygen molecule. Thus, we can conclude that the interaction is between the oxygen molecule and the C59N shell and it results in the shell degradation and carbon atom oxidation at a site neighboring to the nitrogen atom (Fig. 7).

In Fig. 8 we have summarized the results from the NEB calculations of oxygen interacting with the C59N@Fe13 nanoparticle. Our calculations show that the reaction is exothermic with 2.39 eV and is characterized with an activation barrier of 0.11 eV. The exothermic reaction and the low activation barrier suggest that the process can occur spontaneously, and the reaction does not require external driving force to proceed. Thus, the reaction can proceed as a chemical process instead of the electrochemical process. The stable product shows that the reaction is irreversible and as a result the catalyst would not recover.

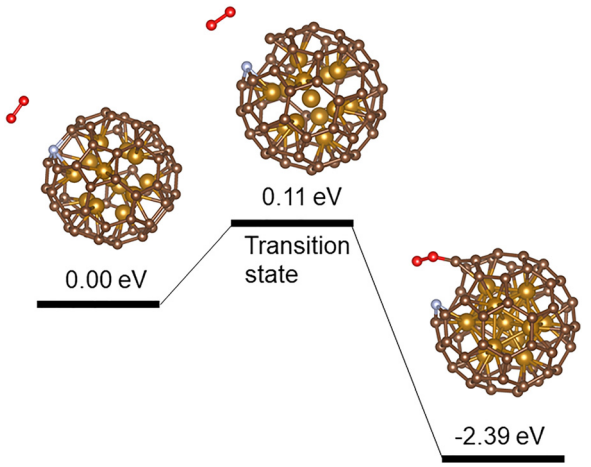

Fig. 8 Molecular oxygen interaction with C59N@Fe13 obtained with the NEB method.

Oxygen can interact with fullerenes chemically, forming oxides like C60O through reactions with O_2, ozone, or atomic oxygen, which can also lead to fragmentation of the fullerene cage or the loss of carbon monoxide.[42,43] Doped fullerenes, like those containing boron or nitrogen, can facilitate oxygen's role in electrocatalysis, particularly in the oxygen reduction reaction. The results in the literature show that such interaction requires either ozone or photoirradiation. Our DFT simulations did not show O_2 activation on fullerene.

To elucidate the size effect of the carbon coated nanoparticle for oxygen reduction we investigate a larger iron cluster, Fe55, coated with a larger fullerene, C180. C180@Fe55 was previously investigated by Taubert *et al.*[32] The Fe55 nanoparticle has icosahedron symmetry and the fullerene is also characterized with icosahedron structure. Thus, C180@Fe55 can be considered as the next member of the class of fullerene coated iron nanoparticles with icosahedron symmetries to which belongs C60@Fe13 as the smallest member. The model is calculated as the C180@Fe55 particle is placed in a periodic cubic box with side of 20 Å. Such model would allow a distance of 1 nm between particles in neighboring cells. In its ground state

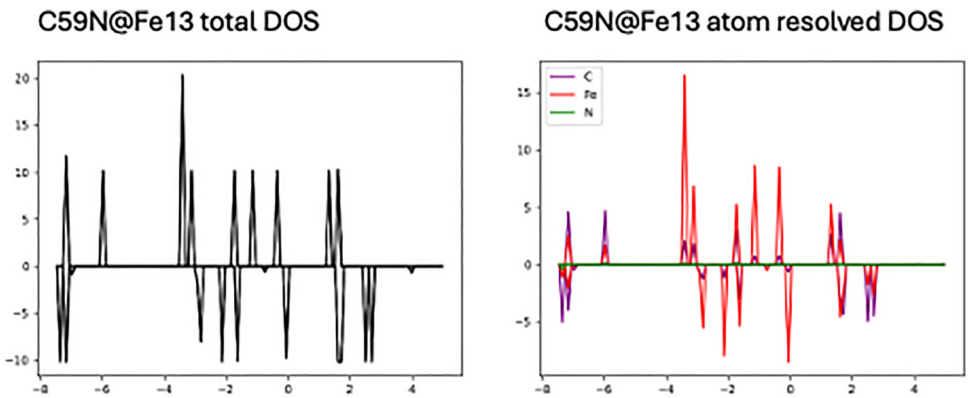

Fig. 7 DOS of iron, carbon and, nitrogen atoms from C59N@Fe13. Spin up and spin down states were plotted for C59N@Fe13.

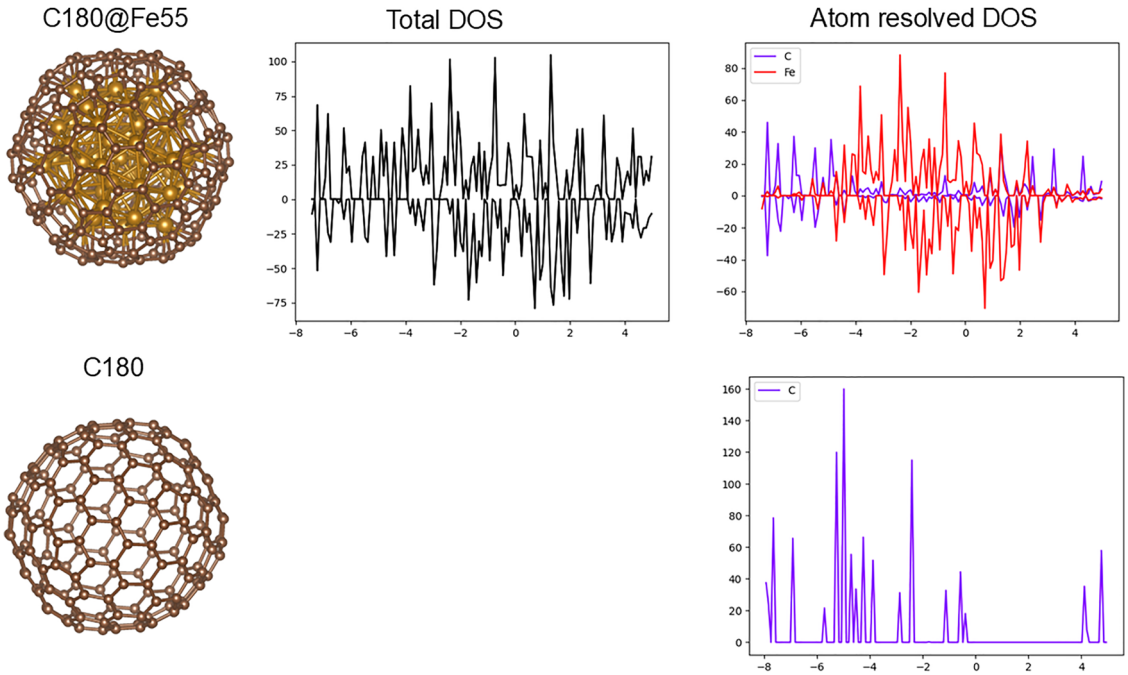

Fig. 9 Optimized geometries and DOS plots for C180@Fe55 and C180. DOS of iron and carbon atoms from C180@Fe55 and C180. Spin up and spin down states were plotted for C180@Fe55.

geometry, every apex iron atom from Fe55 points toward the center of a five-member ring of the fullerene similar to the geometry of C60@Fe13.[32]

Fig. 9 summarizes the optimized geometries and DOS plots for C180@Fe55 and C180. Similar to the C60@Fe13, the DOS plots of the carbon atoms from the surface of C180@Fe55 are very different from the DOS plots of the carbon atoms from the surface of C180. Within the DOS plots of carbon atoms from C180@Fe55 one can distinguish minor peaks which are a result of the hybridization between the iron d-band and the carbon levels. Fe55 has three layers of iron atoms, one central iron atom, 12 iron atoms in the second layer and 42 iron atoms in the outermost layer. While the iron atoms from Fe13 show sharp, discrete DOS peaks due to the particle small size and high symmetry, the iron atoms from Fe55 show more bulk-like energy spectra with clearly defined bands. Bader population analysis shows that 16 electrons are transferred from the iron core of the particle to its carbon shell. When we compare to C60@Fe13 where 7 electrons are transferred to the carbon shell we can conclude that for C60@Fe13 the average charge per surface carbon atom is −0.12 while for C180@Fe55 the average charge per surface carbon atom is −0.09. Thus, with the increase of the particle size we observe a decrease in the negative charge on the particle surface. As the oxygen reduction reaction is an electrophilic process, the reduced charge on the surface might lead to an increase in the activation barrier for surface adsorption of molecular oxygen.

In Fig. 10 we summarize the results for oxygen molecules chemisorbed on the C180@Fe55 surface. We show the obtained geometry, spin density distribution, and electron density difference map. The geometry analysis shows that the oxygen molecule is situated parallel to the surface at a distance of

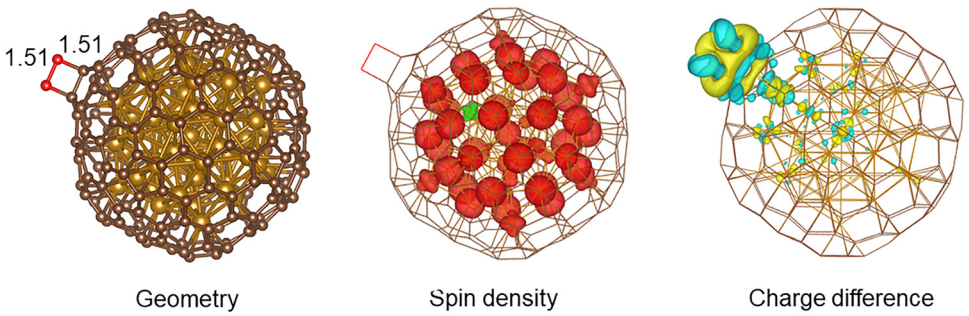

Fig. 10 Geometry and electronic properties of molecular oxygen interaction with C180@Fe55. Blue color denotes positive electron density while yellow color denotes negative electron density. Red color denotes majority spin density, while green color denotes minority spin density. All distances are given in Å.

1.51 Å. The oxygen–oxygen bond length is 1.51 Å which is similar to the bond length of the peroxo species. Fig. 10 summarizes the results for oxygen molecule adsorbed on the edge of a five-member ring. However, on the surface of C180@Fe55 exists another possible adsorption site where the oxygen molecule is adsorbed on the edge of a six-member ring. The oxygen molecule adsorbed on a five-member ring has 0.05 eV lower energy compared to the oxygen molecule adsorbed on a six-membered ring, which shows that both sites are energetically equivalent. The spin density plot in Fig. 10 assigns no spin density to the two oxygen atoms which corresponds to the electronic structure of the peroxo state of the oxygen molecule. The binding energy of the oxygen molecule to the particle surface is −2.97 eV, or 1.5 eV per carbon–oxygen bond. The electron density difference map shown in Fig. 9 verifies that electron density has been transferred from the Fe-core of the C180@Fe55 nanoparticle similar to the C60@Fe13 nanoparticle.

A major difference between the catalyst presented in this study and the widely investigated FeN_3 and FeN_4–graphene catalysts is the structure of the active site. The FeN_3 and FeN_4–graphene catalysts are inspired by the porphyrin chemistry envisioning the active site as exposed metal site coordinated by 3 or 4 pyridinic nitrogen atoms. In this way, the exposed metal can interact and activate molecular oxygen without the formation of stable metal oxide which would poison the active site.[44,45] This study demonstrates a different possible structure where a small metal cluster is encapsulated by a carbon layer. The function of the carbon layer is to prevent the oxidation of the metal cluster while the catalytic properties are transferred to the carbon shell through hybridization between the carbon p_z orbitals and iron d-orbitals. As the Fe–C–N catalyst does not have a precise chemical structure and is usually in an amorphous state with large domains of graphitic carbon, neither of the models could be excluded.

Conclusions

In this work, we employed theoretical methods to investigate the structure and electronic properties of carbon-coated iron nanoparticles comprising iron cores of 13 and 55 atoms, encapsulated by fullerene shells of C60 and C180, respectively. Our results show that the interaction between the iron core and carbon shell is strongly binding, leading to electron density transfer from the iron core to the carbon shell. Density of states analyses reveal hybridization between the iron d-orbitals and the p_z orbitals of the shell carbon atoms. This interaction modifies the electronic structure of the surface carbon atoms, imparting features characteristic of iron d-levels.

We studied the activation of molecular oxygen on the carbon surfaces of these nanoparticles. Our calculations demonstrate that O_2 is sequentially activated to superoxo and peroxo states on the carbon surface with a low activation barrier of 0.64 eV. The overall reaction is slightly endothermic (0.25 eV) and requires an electrochemical driving force. Electron density difference maps indicate that electron transfer originates not only from the surface carbon atoms but also from the iron d-electrons, highlighting a synergistic effect between carbon and iron in facilitating O_2 activation.

We also examined the impact of nitrogen doping, focusing on graphitic nitrogen centers within the carbon shell. Our findings show that molecular oxygen can readily oxidize the C–N bond in such structures, with a strongly exothermic reaction energy (−2.39 eV) and a very low activation barrier (0.11 eV). This process is purely chemical and does not require an electrochemical driving force, suggesting that graphitic nitrogen sites could promote degradation of the carbon-coated iron nanoparticles.

Finally, we found no significant differences in the oxygen activation mechanisms when comparing the smaller C60@Fe13 and the larger C180@Fe55 nanoparticles, indicating that these key processes are robust with respect to nanoparticle size in the range studied.

The calculations show that the onion-like carbon coated iron nanoparticles, observed experimentally in carbon catalysts for electrochemical ORRs, could participate actively in the catalytic reaction and offer an additional active site to the widely accepted single metal sites.

Conflicts of interest

There are no conflict of interest to declare.

Data availability

All data are available upon request from the author.

Acknowledgements

The author acknowledge the support of the World Premier International Research Center Initiative (WPI), Ministry of Education, Culture, Sports, Science, and Technology of Japan (MEXT).

References

1 T. M. Gür, Review of electrical energy storage technologies, materials and systems: challenges and prospects for large-scale grid storage, *Energy Environ. Sci.*, 2018, **11**, 2696–2767.
2 T. Ishihara, Perovskite Oxide for Solid Oxide Fuel Cells. Fuel Cells and Hydrogen Energy, in *Structure and Properties of Perovskite Oxides*, ed. T. Ishihara, Springer, Boston, MA, 2009.
3 A. Chroneos, B. Yildiz, A. Tarancon, D. Parfitt and J. A. Kilner, Oxygen diffusion in solid oxide fuel cell cathode and electrolyte materials: mechanistic insights from atomistic simulations, *Energy Environ. Sci.*, 2011, **4**, 2774–2789.
4 A. Staykov, H. Téllez, T. Akbay, J. Druce, T. Ishihara and J. A. Kilner, Oxygen Activation and Dissociation on Transition

Metal Free Perovskite Surfaces, *Chem. Mater.*, 2015, **27**, 8273–8281.

5 A. Staykov, H. Tellez, J. Druce, J. Wu, T. Ishihara and J. A. Kilner, Electronic properties and surface reactivity of SrO-terminated SrTiO3 and SrO-terminated iron-doped SrTiO3, *Sci. Technol. Adv. Mater.*, 2018, **19**, 221–230.

6 M. A. Laguna-Bercero, J. A. Kilner and S. J. Skinner, Performance and Characterization of (La, Sr)MnO3/YSZ and La0.6Sr0.4Co0.2Fe0.8O3 Electrodes for Solid Oxide Electrolysis Cells, *Chem. Mater.*, 2010, **22**, 1134–1141.

7 G. M. Rupp, A. K. Opitz, A. Nenning, A. Limbeck and J. Fleig, Real-time impedance monitoring of oxygen reduction during surface modification of thin film cathodes, *Nat. Mater.*, 2017, **16**, 640–645.

8 H. Matsumoto, T. Shimura, T. Higuchi, T. Otake, Y. Sasaki, K. Yashiro, A. Kaimai, T. Kawada and J. Mizusaki, Mixed protonic-electronic conduction properties of $SrZr_{0.9-x}Y_{0.1}Ru_xO_{3-\alpha}$, *Electrochemistry*, 2004, **72**, 861–864.

9 Y.-J. Wang, J. Qiao, R. Baker and J. Zhang, Alkaline polymer electrolyte membranes for fuel cell applications, *Chem. Soc. Rev.*, 2013, **42**, 5768–5787.

10 M. Nishihara, L. Christiani, A. Staykov and K. Sasaki, Experimental and theoretical study of charge-transfer complex hybrid polyimide membranes, *J. Polym. Sci., Part B: Polym. Phys.*, 2014, **52**, 293–298.

11 T. Bayer, B. V. Cunning, R. Selyanchyn, M. Nishihara, S. Fujikawa, K. Sasaki and S. M. Lyth, High Temperature Proton Conduction in Nanocellulose Membranes: Paper Fuel Cells, *Chem. Mater.*, 2016, **28**, 4805–4814.

12 T. Bayer, S. R. Bishop, M. Nishihara, K. Sasaki and S. M. Lyth, Characterization of a graphene oxide membrane fuel cell, *J. Power Sources*, 2014, **272**, 239–247.

13 A. A. Gewirth and M. S. Thorum, Electroreduction of Dioxygen for Fuel-Cell Applications: Materials and Challenges, *Inorg. Chem.*, 2010, **49**, 3557–3566.

14 Y. Ha, J. L. Oberst, Z. Zeng, T. T. H. Hoang, Y. Cohen, D. J. Wetzel, R. G. Nuzzo, J. Greeley and A. A. Gewirth, In situ surface stress measurement and computational analysis examining the oxygen reduction reaction on Pt and Pd, *Electrochim. Acta*, 2018, **260**, 400–406.

15 Y. Bing, H. Liu, L. Zhang, D. Ghosh and J. Zhang, Nanostructured Pt-alloy electrocatalysts for PEM fuel cell oxygen reduction reaction, *Chem. Soc. Rev.*, 2010, **39**, 2184–2202.

16 A. Staykov, Y. Ooishi and T. Ishihara, Immobilizing Metal Nanoparticles on Single Wall Nanotubes. Effect of Surface Curvature, *J. Phys. Chem. C*, 2014, **118**, 8907–8916.

17 A. A. Gewirth, J. A. Varnell and A. M. DiAscro, Nonprecious Metal Catalysts for Oxygen Reduction in Heterogeneous Aqueous Systems, *Chem. Rev.*, 2018, **118**, 2313–2339.

18 A. Zitolo, N. Ranjbar-Sahraie, T. Mineva, J. Li, Q. Jia, S. Stamatin, G. F. Harrington, S. M. Lyth, P. Krtil, S. Mukerjee, E. Fonda and F. Jaouen, Identification of catalytic sites in cobalt-nitrogen-carbon materials for the oxygen reduction reaction, *Nat. Commun.*, 2017, **8**, 957.

19 S. M. Lyth, Y. Nabae, S. Moriya, S. Kuroki, M. Kakimoto, J. Ozaki and S. Miyata, Carbon Nitride as a Nonprecious Catalyst for Electrochemical Oxygen Reduction, *J. Phys. Chem. C*, 2009, **113**, 20148–20151.

20 Z. Chen, D. Higgins, A. Yu, L. Zhang and J. Zhang, A review on non-precious metal electrocatalysts for PEM fuel cells, *Energy Environ. Sci.*, 2011, **4**, 3167–3192.

21 J. A. Varnell, E. C. M. Tse, C. E. Schulz, T. T. Fister, R. T. Haasch, J. Timoshenko, A. I. Frenkel and A. A. Gewirth, Identification of carbon-encapsulated iron nanoparticles as active species in non-precious metal oxygen reduction catalysts, *Nat. Commun.*, 2016, **7**, 12582.

22 J. Liu, D. Takeshi, K. Sasaki and S. M. Lyth, Defective Graphene Foam: A Platinum Catalyst Support for PEMFCs, *J. Electrochem. Soc.*, 2014, **161**, F838–F844.

23 A. Garsuch, R. Yang, A. Bonakdarpour and J. R. Dahn, The effect of boron doping into Co-C-N and Fe-C-N electrocatalysts on the oxygen reduction reaction, *Electrochim. Acta*, 2008, **53**, 2423–2429.

24 Y. Ji, H. Dong, C. Liu and Y. Li, The progress of metal-free catalysts for the oxygen reduction reaction based on theoretical simulations, *J. Mater. Chem. A*, 2018, **6**, 13489–13508.

25 L. Dai, Y. Xue, L. Qu, H.-J. Choi and J.-B. Baek, Metal-Free Catalysts for Oxygen Reduction Reaction, *Chem. Rev.*, 2015, **115**, 4823–4892.

26 A. Sarapuu, E. Kibena-Põldsepp, M. Borghei and K. Tammeveski, Electrocatalysis of oxygen reduction on heteroatom-doped nanocarbons and transition metal–nitrogen–carbon catalysts for alkaline membrane fuel cells, *J. Mater. Chem. A*, 2018, **6**, 776–804.

27 N. A. M. Barakat, A. G. El-Deen, Z. K. Ghouri and S. Al-Meer, Stable N-doped & FeNi-decorated graphene non-precious electrocatalyst for Oxygen Reduction Reaction in Acid Medium, *Sci. Rep.*, 2018, **8**, 3757.

28 S. Liu, Z. Yang, M. Li, W. Lv, L. Liu, Y. Wang, X. Chen, X. Zhao, P. Zhu and G. Wang, Facile synthesis of 3D hierarchical mesoporous Fe-C-N catalysts as efficient electrocatalysts for oxygen reduction reaction, *Int. J. Hydrocarbon Eng.*, 2018, **43**, 5163–5174.

29 J. Bartelmess and S. Giordani, Carbon nano-onions (multilayer fullerenes): chemistry and applications. Beilst, *J. Nanotechnol.*, 2014, **5**, 1980–1998.

30 O. Mykhailiv, H. Zubyk and M. E. Plonska-Brzezinska, Carbon nano-onions: Unique carbon nanostructures with fascinating properties and their potential applications, *Inorg. Chim. Acta*, 2017, **468**, 49–66.

31 W.-J. Jiang, L. Gu, L. Li, Y. Zhang, X. Zhang, L.-J. Zhang, J.-Q. Wang, J.-S. Hu, Z. Wei and L.-J. Wan, Understanding the High Activity of Fe–N–C Electrocatalysts in Oxygen Reduction: Fe/Fe3C Nanoparticles Boost the Activity of Fe–Nx, *J. Am. Chem. Soc.*, 2016, **138**, 3570–3578.

32 S. Taubert and K. Laasonen, The molecular and magnetic structure of carbon-enclosed and partially covered Fe55 particles, *Phys. Chem. Chem. Phys.*, 2014, **16**, 3648–3660.

33 G. Kresse and J. Hafner, Ab initio, *Phys. Rev. B: Condens. Matter Mater. Phys.*, 1993, **47**, 558–561.

34 G. Kresse and J. Furthmüller, Efficient iterative schemes for ab initio total-energy calculations using a plane-wave basis

set, *Phys. Rev. B: Condens. Matter Mater. Phys.*, 1996, **54**, 11169–11186.

35 G. Kresse and J. Furthmüller, Efficiency of ab-initio total energy calculations for metals and semiconductors using a plane-wave basis set, *Comput. Mater. Sci.*, 1996, **6**, 15–50.

36 P. E. Blöchl, Projector augmented-wave method, *Phys. Rev. B: Condens. Matter Mater. Phys.*, 1994, **50**, 17953–17979.

37 W. Tang, E. Sanville and G. Henkelman, A grid-based Bader analysis algorithm without lattice bias, *J. Phys.: Condens. Matter*, 2009, **21**, 084204.

38 K. Momma and F. Izumi, VESTA 3 for three-dimensional visualization of crystal, volumetric and morphology data, *J. Appl. Crystallogr.*, 2011, **44**, 1272–1276.

39 A. Staykov, T. Nishimi, K. Yoshizawa and T. Ishihara, Oxygen Activation on Nanometer-Size Gold Nanoparticles, *J. Phys. Chem. C*, 2012, **116**, 15992–16000.

40 H. Miao, S. Li, Z. Wang, S. Sun, M. Kuang, Z. Liu and J. Yuan, Enhancing the pyridinic N content of Nitrogen-doped graphene and improving its catalytic activity for oxygen reduction reaction, *Int. J. Hydrocarbon Eng.*, 2017, **42**(47), 28298–28308.

41 Y. Li, H. Yadegari, X. Li, M. N. Banis, R. Li and X. Sun, Superior catalytic activity of nitrogen-doped graphene cathodes for high energy capacity sodium–air batteries, *Chem. Commun.*, 2013, **49**(100), 11731–11733.

42 R. C. Chapleski Jr., J. R. Morris and D. Troya, A theoretical study of the ozonolysis of C60: primary ozonide formation, dissociation, and multiple ozone additions, *Phys. Chem. Chem. Phys.*, 2014, **16**, 5977–5986.

43 D. Heymann, S. M. Bachilo, R. B. Weisman, F. Cataldo, R. H. Fokkens, N. M. M. Nibbering, R. D. Vis and L. P. Felipe Chibante, C60O3, a Fullerene Ozonide: Synthesis and Dissociation to C60O and O_2, *J. Am. Chem. Soc.*, 2000, **122**, 11473–11479.

44 P. Yuan, C. Li, J. Zhang, F. Wang, J. Wang and X. Chen, The nearby atomic environment effect on an Fe–N–C catalyst for the oxygen reduction reaction: a density functional theory-based study, *Phys. Chem. Chem. Phys.*, 2024, **26**, 6826–6833.

45 T. Zheng, J. Wang, Z. Xia, G. Wang and Z. Duan, Spin-dependent active centers in Fe–N–C oxygen reduction catalysts revealed by constant-potential density functional theory, *J. Mater. Chem. A*, 2023, **11**, 19360–19373.